Inorganic Chemistry

Article

pubs.acs.org/IC

Theoretical ^{57}Fe Mössbauer Spectroscopy for Structure Elucidation of [Fe] Hydrogenase Active Site Intermediates

Joël Gubler, Arndt R. Finkelmann, and Markus Reiher*

Laboratorium für Physikalische Chemie, ETH Zürich, Wolfgang-Pauli-Strasse 10 8093 Zürich, Switzerland

Supporting Information

ABSTRACT: [Fe] hydrogenase is a hydrogen activating enzyme that features a monoiron active site, which can be well characterized by Mössbauer spectroscopy. Mössbauer spectra have been measured of the CO and CN^- inhibited species as well as under turnover conditions [Shima, S. et al., *J. Am. Chem. Soc.*, **2005**, *127*, 10430]. This study presents calculated Mössbauer parameters for various active-site models of [Fe] hydrogenase to provide structural information about the species observed in experiment. Because theoretical Mössbauer spectroscopy requires the parametrization of observables from *first-principles* calculations (i.e., electric-field gradients and contact densities) to the experimental observables (i.e., quadrupole splittings and isomer shifts), nonrelativistic and relativistic density functional theory methods are parametrized against a reference set of Fe complexes specifically selected for the application to the Fe center in [Fe] hydrogenase. With this methodology, the measured parameters for the CO and CN^- inhibited complexes can be reproduced. Evidence for the protonation states of the hydroxyl group in close proximity to the active site and for the thiolate ligand, which could participate in proton transfer, is obtained. The unknown resting state measured in the presence of the substrate and under pure H_2 atmosphere is identified to be a water-coordinated complex. Consistent with previous assignments based on infrared and X-ray absorption near-edge spectroscopy, all measured Mössbauer data can be reproduced with the active site's iron atom being in oxidation state +2.

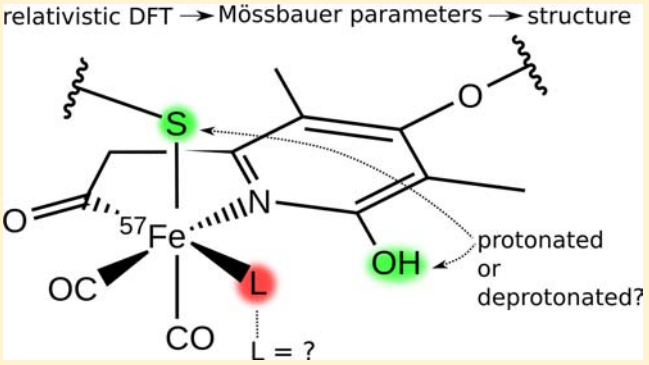

1. INTRODUCTION

[Fe] hydrogenase[1−3] catalyzes the reversible reduction of N^5,N^{10}-methenyltetrahydromethanopterin (methenyl-H_4MPT$^+$) with H_2 to form N^5,N^{10}-methylenetetrahydromethanopterin (methylene-H_4MPT) and a proton (compare Figure 1),

$$\text{methenyl-H}_4\text{MPT}^+ + \text{H}_2 \xrightleftharpoons{\text{[Fe]hydrogenase}} \text{methylene-H}_4\text{MPT} + \text{H}^+$$

This reaction is part of the reduction pathway of CO_2 to methane in methanogenic archaea.[4,5] [Fe] hydrogenase catalyzes various proton exchange reactions only in the presence of the substrate methenyl-H_4MPT$^+$[5,6] and is inhibited by high concentrations of CO and CN^-[5,7] and by isocyanides.[8,9]

Other types of hydrogenases, namely, [FeFe] and [NiFe] hydrogenases, catalyze the direct reversible oxidation of H_2.[10] In contrast to [NiFe] and [FeFe] hydrogenases, whose active sites consist of polynuclear metal centers,[11] [Fe] hydrogenase features a monoiron active site. Its metal cofactor was discovered 14 years after the discovery of the enzyme.[12] The structure of the cofactor (iron-guanylylpyridone; in short, FeGP) is depicted in Figure 1. IR spectroscopy identified the Fe atom to be ligated by two carbonyl ligands.[7] In the CO inhibited form, the iron atom is coordinated by an additional CO ligand, and in the cyanide inhibited form, it ligates an additional CN^- ligand.[7] The IR study[7] suggests that the

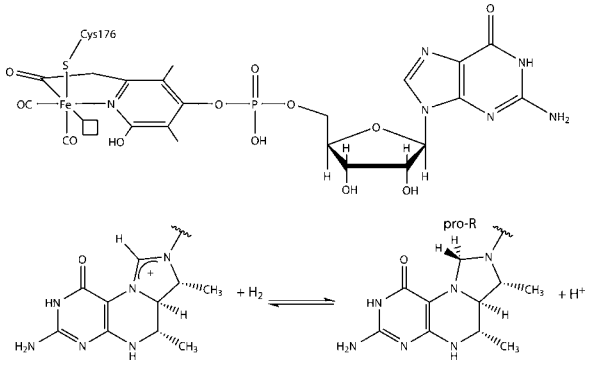

Figure 1. (top) Lewis structure of the FeGP cofactor constituting the active site of [Fe] hydrogenase. The open coordination site in the sixth position, where catalysis is believed to proceed, is marked by a box. (bottom) Reaction catalyzed by [Fe] hydrogenase. Methenyl-H_4MPT$^+$ and dihydrogen (left) react to methylene-H_4MPT and a proton (right).

Received: August 20, 2013
Published: November 20, 2013

   dx.doi.org/10.1021/ic4021349 | *Inorg. Chem.* 2013, 52, 14205−14215

oxidation state of the iron atom is likely to be +2. Paramagnetic oxidation states could be excluded based on magnetic measurements. Furthermore, the enzyme is EPR silent throughout catalysis.[13] Mössbauer spectra favor a low oxidation state but could not unequivocally assign it to be low-spin Fe(0) or low-spin Fe(II).[13] An IR spectroscopy study by Wang et al. favored Fe(II) by comparison to various related complexes.[14] This assignment is in line with a recent X-ray absorption near-edge spectroscopy study[15] and is the currently accepted oxidation state. For comparison, in active [NiFe] hydrogenases, the oxidation state of the active-site iron atom is Fe(II), and in active [FeFe] hydrogenases, the oxidation state of the iron atoms can be Fe(I) and Fe(II).[16]

The first crystal structure of the apoenzyme was solved by Pilak et al.[17] The holoenzyme structure was initially solved by Shima et al.[18] Later, the active site structure was refined for a mutated enzyme containing the FeGP cofactor.[19] The iron atom turned out to be in an octahedral ligand environment. It is coordinated by the nitrogen atom of a pyridone derivative, by a cysteine ligand, and by two carbonyl ligands in the square plane and an acyl ligand in the apical position. The binding site *trans* to the acyl ligand (position six) is the putative open coordination site enabling coordination of H_2 for catalysis (see Figure 1). Although the active sites of [FeFe] and [Fe] hydrogenase are seemingly different, the catalytic iron center carries the same type of ligands in the same geometric arrangement.[20] In the crystal structure, a weakly bound solvent molecule (most likely water) is in the sixth position.[18,19]

H_2 activation by [Fe] hydrogenase is still a matter of discussion, and several mechanisms were proposed over the years.[3] Crystallization of a C176A mutated enzyme with the substrate methenyl-H_4MPT$^+$ facilitated the elucidation of the mechanism.[21] It was suggested that methenyl-H_4MPT$^+$ binds in the *open* conformation of the enzyme, which then transitions into the *closed* conformation where H_2 is split and methenyl-H_4MPT$^+$ is reduced by hydride transfer. Opening of the enzyme and dissociation of methylene-H_4MPT closes the catalytic cycle.[19] A detailed atomistic mechanism was then proposed by Yang and Hall[22] on the basis of density functional theory (DFT) calculations. These authors proposed a hydride species as possible resting state in the presence of H_2. Our reinvestigation with dispersion-corrected density functionals confirmed the essential features of the Yang−Hall mechanism, predicted a fast hydride transfer from Fe to methenyl-H_4MPT$^+$, and provided detailed insights into the kinetics.[23]

Still, some questions regarding the active site of [Fe] hydrogenase remain open. The resting state of the enzyme, which has been measured by Mössbauer spectroscopy, is not well-defined. That is the protonation states, especially those of the cysteinate ligand and the hydroxyl group of the pyridone, are not known. These sites may serve as base during catalysis.[21,22] Moreover, the identity of the ligand that may occupy the free coordination site under reaction conditions (i.e., H_2 atmosphere and presence of methenyl-H_4MPT$^+$) is unknown. However, these are crucial ingredients for a full understanding of the catalytic mechanism. The resting state is the starting point for catalytic action. The protonation states of the ligands may give hints on possible protonation/deprotonation pathways. These issues could be resolved by Mössbauer measurements combined with quantum chemical calculations.

Mössbauer spectroscopy is a versatile tool for investigating properties of iron compounds enriched with ^{57}Fe. It can yield details on the electronic structure of the Fe atom (oxidation state) and is sensitive to the chemical environment of the iron nucleus.[24] However, interpretation of Mössbauer spectra is mostly done in an indirect way by comparing to Mössbauer parameters of known compounds, which limits its versatility. By contrast, quantum chemical calculations can provide Mössbauer parameters for iron complex structures optimized *in silico*. By comparison to the experimental results, an identification of the measured species should be feasible.

For an unambiguous identification of the species measured by Mössbauer spectroscopy,[13] we calculate Mössbauer parameters for models of the [Fe] hydrogenase active site in this work. Several intermediates were proposed for the catalytic mechanism and the resting state.[21,22] They differ in (i) protonation state of the thiolate ligand, (ii) protonation state of the pyridone's hydroxyl group, and (iii) the identity of the ligand in the putative binding site, which could be H_2O, OH^-, H^-, or H_2. The H^--coordinated complex, which is the product of H_2 cleavage in the Hall mechanism, can also be described as a complex that features a strong Fe−$H^{\delta-}\cdots H^{\delta+}$−O dihydrogen bond (1.382 Å compared with 0.786 Å for bound H_2[22]) if the pyridone's hydroxyl group carries a proton.[22] A vacant binding site is also possible and therefore considered here as well. These variants are depicted in Figure 2. Especially, the inspection of a hydride ligand is appealing since Mössbauer spectra were also measured under catalytic conditions[13] and the role of the metal for catalysis has not been definitively clarified yet.

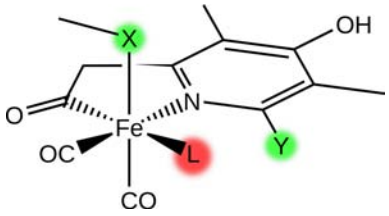

Figure 2. Lewis structure of our active-site model complex. "X" represents a thiolate ligand (cysteinate in the protein) and "Y" represents a hydroxyl group, both marked in green. The protonation states of these ligands and the identity of the ligand in the putative binding site for external ligands (sixth position, marked in red) are modified to give rise to different active-site variants. L was chosen to be either H_2O, OH^-, H^-, or H_2 or left as an open coordination site.

The *first-principles* calculation of Mössbauer parameters requires a calibration of the methodology, as will be outlined in the next section. For this purpose a tailored reference set was compiled, especially designed to contain complexes closely related to the active site of [Fe] hydrogenases (section 3.1). Nonrelativistic and recently developed relativistic DFT methods[25] are applied. They are described in detail in the computational methodology section 3.2. With the calibration established in section 4.1, Mössbauer parameters calculated for [Fe] hydrogenase model complexes are discussed and assessed in sections 4.2 and 4.3, respectively.

2. THEORY

The two main quantities measured in Mössbauer spectroscopy are the isomer shift, δ, and the quadrupole splitting, Δ.[24] The isomer shift δ originates from the different electronic environment of the absorber nucleus compared with that of the emitter nucleus and thus contains information on the oxidation state and the chemical composition of the surrounding, that is, on the coordination sphere and type of

dx.doi.org/10.1021/ic4021349 | *Inorg. Chem.* 2013, 52, 14205−14215

Table 1. Reference Set for the Calculation of Mössbauer Parameters[a]

no.	complex[b]	structure	N	OS	$2S+1$	δ_{exp}[c] (mm/s)	Δ_{exp} (mm/s)	η_{exp}	T (K)	ref
a	$[Fe(CO)_5]$	ref 28	5	0	1	−0.09(1)[d]	2.57(1)		78	52
b	$[Fe(\eta^4\text{-butadiene})(CO)_3]$	ref 53	7	0	1	0.12	−1.34	0.4	4.2	30
c	*trans*-$[Fe(cyclam)(N_3)_2]^+$	ref 28	6	III	2	0.28(6)	−2.24(1)	0.4[e]	80	54
d	$[Fe{=}O(tmc)(NCCH_3)]^{2+}$	ref 28	6	IV	3	0.17(1)	1.24(1)	0.5	4.2	55
e	$[Fe(por)(O_2)]^-$	ref 28	5	III	6	0.67	0.62		4.2	56
f	$[Fe(NO)(pyS_4)]^+$	ref 28	6	II	1	0.04(2)	−1.63(2)	0.9(1)	80	57
g	$[Fe(NO)(pyS_4)]$	ref 28	6	II	2	0.33(2)	−0.40(2)	0.3(3)	80	57
h	$[Fe(PH_3)(pyS_4)]$	ref 28	6	II	1	0.34(2)	0.69(2)	0.9(1)	80	57
i	$[Fe(SMe_3)(pyS_4)]$	ref 28	6	II	1	0.44(2)[f]	0.43(2)[f]	0.1(1)[f]	80	57
j	$[Fe(PyO)I(CO)_2PPh_3]$	ref 50	6	II	1	0.10(2)	0.48(2)	0.0[g]	55	50
k	$[Fe(PyO)I(ArS)(CO)_2PPh_3]$	none	6	II	1	0.06(2)	−0.83(2)	0.6(2)[g]	100	51
l	$[Fe(PyS)I(CO)_2PPh_3]$	none	6	II	1	0.10(2)	−0.35(3)	0.0(5)[g]	77	51
m	$[Fe(SC_5H_4N\text{-}CO)I(CO)_2(ArNC)]$	ref 58	6	II	1	0.01(2)	0.29(2)	0.6(4)[g]	77	51
n	$[Fe(PyS)(ac)(CO)_2]_2$	ref 59	6	II	1	0.06(1)	−0.74(2)	0.4(1)[g]	77	51
o	$[Fe(Pys)(ac)(CO)_2(ArNC)]$[h]	none	6	II	1	0.00(2)	0.73(2)	0.5(1)[g]	100	51
p	$[Fe(PyS)(ac)(CO)_2PPh_3]$	ref 59	6	II	1	0.00(2)	−1.14(2)	0.4(1)[g]	77	51
q	$[Fe(PyS)(ac)(CN)(CO)_2]^-$[h]	none	6	II	1	−0.02(2)	0.89(2)	0.1(1)[g]	77	51

[a]The set contains compounds with different coordination number (N), oxidation state (OS), and spin multiplicity, $2S+1$. "Structure" denotes the source for the initial structure that was then subject to structure optimization. Where available, the precision of the experimental data is given in parentheses. [b]Abbreviations: ac, CH_3CO^-; por, porphyrin; ArNC, 2,6-Me_2-C_6H_3NC; ArS, 2,6-$Me_2C_6H_3S$; PyO, 6-methyl-2-pyridonate; PyS, 6-methyl-pyridyl-2-thiolate; pyS_4, dianion of 2,6-bis(2-mercaptophenylthiomethyl)pyrdidine; tmc, 1,4,8,11-tetramethyl-1,4,8,11-tetraazacyclotetradecane. [c]Isomer shift relative to α-Fe metal at room temperature. [d]In ref 52, the isomer shift is given with respect to nitroprusside and therefore in this work is corrected by −0.26 mm/s.[24] [e]η_{exp} measured at 160 K. [f]The experimental values are for the dinuclear species $[Fe(PyS_4)]_2$ that contains two μ-thiolate bridges[57] [g]η_{exp} measured at 5 K. [h]Different isomer than suggested in original literature, see Supporting Information for a detailed discussion.

ligands. It can be calculated as a function of the electron density at the position of the nucleus, the so-called contact density, $\rho(0)$, of the absorber "(a)" and emitter (source "(s)") atoms.[26]

$$\delta = \frac{c}{E_\gamma}\frac{3}{5}\frac{Ze^2}{\varepsilon_0}R^2\left(\frac{\Delta R}{R}\right)[\rho^{(a)}(0) - \rho^{(s)}(0)] \quad (1)$$

Here, δ is the isomer shift expressed as a Doppler velocity (mm/s), c the speed of light (c = 299792458 m/s), E_γ the energy of the nuclear transition of an isolated nucleus (E_γ = 14.4 keV[24]), Z the nuclear charge number, e the elementary charge, ε_0 the vacuum permittivity, R the average charge radius of the nucleus, and ΔR the difference between the charge radii of the excited and ground state nucleus.

In order to compare isomer shift values measured with different γ-sources, isomer shifts are generally reported relative to the isomer shift of α-iron.[24] All quantities in front of the square brackets in eq 1 are constant for a given isotope and can be collected in the so-called isomer shift calibration constant, α,

$$\delta = \alpha[\rho^{(a)}(0) - \rho^{(s)}(0)] \quad (2)$$

The prefactor α is not measured or calculated directly. However, the isomer shift depends linearly on the contact density of the absorber $\rho^{(a)}(0)$ since the contact density of the emitter $\rho^{(s)}(0)$ is constant for the same source. Hence, calculated contact densities of known complexes can be parametrized to experimental isomer shifts to establish a linear relationship between contact density and isomer shift,

$$\delta_{exp} = a\rho^{(a)}(0) + b \quad (3)$$

(accordingly, we will drop the superscript (a) in the equations and tables to come). Since the calculated contact density is highly dependent on the computational protocol,[27−29] this calibration has to be done for every quantum chemical approximation (i.e., density functional and basis set chosen). A reliably calibrated linear relation can then efficiently be used to predict isomer shifts on the basis of calculated contact densities.

The quadrupole splitting, Δ, arises from the interaction of the quadrupole moment of the excited state of the ^{57}Fe nucleus, which possesses a nuclear spin of 3/2, with the electric field gradient (EFG) at the nucleus. The quadrupole splitting can be calculated according to[24]

$$\Delta = \frac{c}{E_\gamma}\frac{eQV_{zz}}{2}\sqrt{1 + \frac{\eta^2}{3}} \quad (4)$$

where Q is the electric quadrupole moment of the ^{57}Fe nucleus in barn (see the Supporting Information for a detailed presentation of unit conversions). The principal values V_{ii} of the EFG tensor are assigned according to their absolute value in such a way that $|V_{xx}| \le |V_{yy}| \le |V_{zz}|$. The asymmetry parameter η is defined as

$$\eta = \frac{V_{xx} - V_{yy}}{V_{zz}}. \quad (5)$$

The V_{ii} can be obtained from quantum chemical calculations. Different approaches exist to solve eq 4. They are based on literature values for Q,[30−32] which, however, scatter around a value of 0.15 b (b = barn),[33] or Q is parametrized to a reference set of molecules. The latter can be accomplished with a linear form of eq 4,

$$\Delta_{exp} = a\left(\frac{c}{E_\gamma}\frac{eV_{zz}}{2}\sqrt{1 + \frac{\eta^2}{3}}\right) + b \quad (6)$$

so that the slope a, which can be obtained by linear regression, is identical to the nuclear quadrupole moment Q. The artificially introduced parameter b may also be considered as

dx.doi.org/10.1021/ic4021349 | Inorg. Chem. 2013, 52, 14205−14215

an adjustable parameter,[34−37] or it can be set to zero.[38,39] In this work, both options are considered.

3. COMPUTATIONAL PROTOCOL

3.1. Reference Set of Fe Complexes. A variety of reference sets have been employed in the literature to calibrate isomer shift and quadrupole splitting calculations.[28,32,35−38,40−44] Here, we provide another one, tailor-made to calibrate the equations for the Mössbauer parameters, given in the previous section, for the [Fe] hydrogenase active site. Our selection is based on several considerations. Most reference sets contain small anionic complexes, like $[Fe(Cl)_4]^{2-}$.[45] For these complexes, the counterions present in the crystal, on which the experiment is carried out, can be close to the iron atom and can thus affect the Mössbauer parameters.[45−48] It is in general difficult to calculate the electronic structure of isolated small anions. Diffuse basis functions are necessary to describe the extended electron density, and electron leakage from such highly charged anions is likely to be observed. In the crystal, the complexes might also be distorted such that the symmetry is lowered compared with the isolated complexes optimized in the calculations. As a consequence, we refrain from including such small anionic complexes in our reference set (large anionic complexes are included).

Another consideration is that the experimental isomer shifts and quadrupole splittings are temperature dependent because of vibrations in the crystal.[24,49] Since our calculations do not incorporate temperature effects, we only take into account experimental data measured below 100 K, for which the sign of the quadrupole splitting was determined as well. Moreover, experimental Mössbauer data are available for biomimetic model complexes of [Fe] hydrogenase with variations in the ligand sphere.[50,51] Because it is desirable to calibrate to complexes with structural similarity to the active site of the enzyme, they were included in the reference set. The complete reference set is shown in Table 1.

3.2. Computational Methodology. If available the crystal structure or a computationally optimized structure taken from the literature was the starting point for our structure optimizations. For some complexes, no reference structure was available. These were optimized from the structure suggested in the corresponding article. [Fe] hydrogenase models were derived from the crystal structure of [Fe] hydrogenase from *Methanocaldococcus jannaschii* (PDB code 3F47)[19] and then optimized. All structures were fully optimized with the TPSS exchange-correlation functional,[60] the def2-TZVP basis set on all atoms,[61] Grimme's DFT-D3 dispersion correction,[62] and the conductor-like screening model (COSMO) for electrostatic screening[63] with a dielectric constant of $\varepsilon = 78$ in order to be consistent with the literature.[28,64] For iodine, the only group-5 element in the reference complexes, the effective core potential def2-ecp, which is a modified version of the one reported by Peterson et al.,[61,65] was utilized. Structure optimizations were conducted with the Turbomole suite of programs[66,67] (version 6.3.1). To speed up the calculations, the resolution of the identity (RI) approximation was invoked with the corresponding auxiliary basis set[68] as implemented in Turbomole. The convergence criteria were set to 10^{-4} hartree/bohr for the length of the gradient vector that collects all first-order partial derivatives of the electronic energy with respect to the nuclear coordinates and to 10^{-7} hartree for the electronic energy. Structures obtained with the TPSS exchange-correlation functional were shown to be accurate for isomer shift calculations.[28] A similar methodology was successfully applied by other groups.[28,32,35,37,39,69]

For the calculation of Mössbauer parameters, accurate contact densities and EFGs are decisive. Consequently, large basis sets with uncontracted s-functions have to be applied in order to increase the flexibility in the core region.[28,29,32,40,41,70] Furthermore, a numerical quadrature procedure for the radial functions, which is accurate not only in the valence but also in the core region, is important.[40] In this study, calculations of the contact density and EFG were performed with the Molcas program package (version 7.8)[71] and the B3LYP exchange-correlation functional[72−74] with the VWN5 parametrization,[75] which is well suited for the calculation of Mössbauer parameters of iron complexes (except for polynuclear and ferrocene-like complexes).[37,41] For the nonrelativistic calculations, the Fe basis set of Fux et al.,[76] which closely resembles the CP(PPP) basis set of Neese,[40] and the def2-TZVP basis set on all other atoms[61] were chosen. For the numerical integration, an ultrafine grid in conjunction with the radial quadrature scheme of Lindh, Malmqvist, and Gagliardi[77] assured high accuracy. We exploited an undocumented keyword "Mossbauer" in the "Grid Input Block" in Molcas 7.8, which increases the number of grid points at the Mössbauer nucleus.

In the Molcas calculations, the polarizable continuum model (PCM)[78,79] with ε again set to 78 was invoked to model electrostatic screening. We found choosing $\varepsilon = 4$ to have a negligible effect on the calculated contact densities and EFG (based on a comparison employing the same structures; see Supporting Information).

In the relativistic calculations, the special Fe basis set developed by Mastalerz et al.[29] for Mössbauer calculations was chosen. For the atoms directly bound to the iron center the ANO-RCC basis set with a triple-ζ contraction scheme including polarization functions and for all other atoms one with a double-ζ contraction[80] including polarization functions were employed. The Dirac Hamiltonian and the property operators were decoupled with the Douglas−Kroll−Hess decoupling scheme to the 20th order DKH(20,20).[27,81−87] At this high order, exact decoupling has been achieved for the iron complexes under consideration. As any exact decoupling methodology would be hardly feasible for the large molecules under consideration here, the recently developed local approximation to the unitary decoupling transformation (DLU) was invoked.[25] Results for main group elements suggest that spin−orbit coupling can be neglected in the calculation of electric field gradients at iron nuclei,[88] and thus a scalar-relativistic approach was adopted. The numerical integration scheme was the same as for the nonrelativistic case.

Tight convergence criteria were applied for the self-consistent field iterations to produce the orbitals from which the properties are calculated: electronic energy difference smaller than 10^{-10} hartree, the difference in density-matrix and Fock-matrix elements smaller than 10^{-5} and 10^{-7} atomic units, respectively, and the norm of the orbital displacement vector smaller than 0.2×10^{-5} atomic units in the DIIS procedure. The iron basis sets and further remarks on the calculations are described in detail in the Supporting Information.

In the nonrelativistic property calculations, we have chosen a point-like nucleus for the iron atom because it has become a standard choice.[40] We should note, however, that point-like nuclei feature a cusp in the electron density at the position of the nucleus in nonrelativistic theory (and they lead to weak but integrable singularities in relativistic theory). This feature is notoriously difficult (if not impossible) to describe by Gaussian basis functions, which feature a zero slope at their origin. Moreover, the cusp is an artifact of the point-nucleus model because "physical" atomic nuclei possess a finite charge distribution, which does not create a cusp in the electron density, neither in nonrelativistic nor in relativistic theory. However, the error introduced by a point-like nucleus is atom-like and mostly conserved, that is, transferable from molecule to molecule. Consequently, this error leads to a constant shift of the contact density, which is captured by the calibration parameters. Nevertheless, we chose Gaussian finite nuclei in the relativistic calculations as such calculations are more sensitive to the choice of the nuclear potential. By construction, they are also more accurate than nonrelativistic calculations and should thus be accompanied by the more consistent model for the extended nuclear charge distribution (see refs 27, 70, and 89 for details).

Relative electronic energies of structural isomers are given in section 4.2 for the TPSS-D3 setup and thus correspond to the optimized structures. Electronic energy differences calculated with the B3LYP functional within the relativistic setup in Molcas are found to be consistently higher by about 14−25 kJ/mol (this effect is owed to the choice of a different functional in the relativistic setup). However, we found in the H^--coordinated complex one exception for which the difference between B3LYP and TPSS-D3 results turned out to be much higher than 25 kJ/mol. While we can exclude any technical problems that might have led to the deviation, we note that the H^--

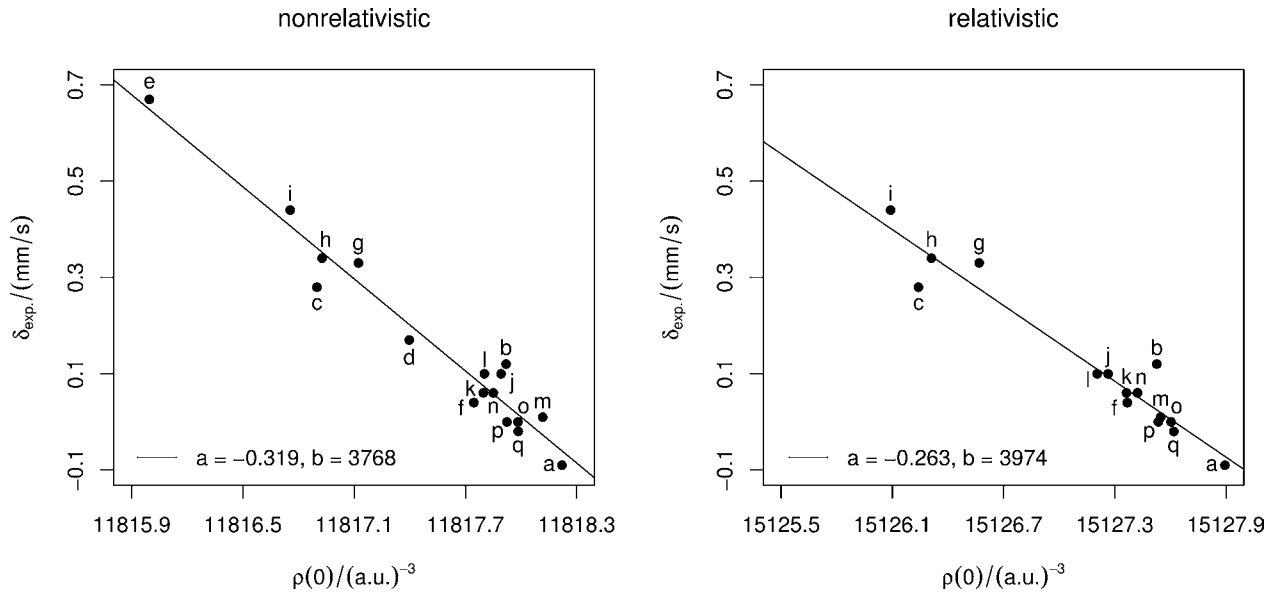

Figure 3. Linear regressions for the nonrelativistic (left panel) and relativistic (right panel) isomer shifts according to eq 3.

Table 2. Regression Parameters *a* and *b* for Nonrelativistic and Relativistic Calculations of Mössbauer Parameters

N^a	method^b	a^c	b^c (mm/s)	R^2	RMSD^d (mm/s)
		Isomer Shift			
17	NR	−0.31887(1833) (bohr^3·mm/s)	3768.409(216596)	0.95	0.044
15^e	NR	−0.31059(2575) (bohr^3·mm/s)	3670.543(304340)	0.92	0.046
15	R	−0.26268(1941) (bohr^3·mm/s)	3973.703(293678)	0.93	0.042
		Quadrupole Splitting			
17	NR	0.13999(1790) (b)	0.000^f	0.79	0.54
17	NR	0.13993(1847) (b)	−0.027(137)	0.79	0.56
15^e	NR	0.14342(1793) (b)	0.000^f	0.82	0.52
15	R	0.15234(1151) (b)	0.000^f	0.93	0.33
15	R	0.15154(1122) (b)	−0.112(84)	0.93	0.33

$^a N$ = number of complexes included in the fit. ^{b}NR = nonrelativistic; R = relativistic. ^{e}The numbers in parentheses denote the standard deviations obtained for the fit parameters (e.g., 3768.409(216596) implies 3768.409 ± 216.596). ^{d}Calculated as standard deviation of the residuals $(\sum_{i=1}^{N_{sample}}(y_i - \hat{y}_i)^2/N_{free})^{1/2}$; with $N_{free} = N_{sample} - N_{parameters}$, y_i being the data points, and $\hat{y}_i$ being the predicted value). ^{e}Only complexes converged in the relativistic calculations. $^f b$ = 0.000 mm/s enforced by eliminating b as an adjustable parameter.

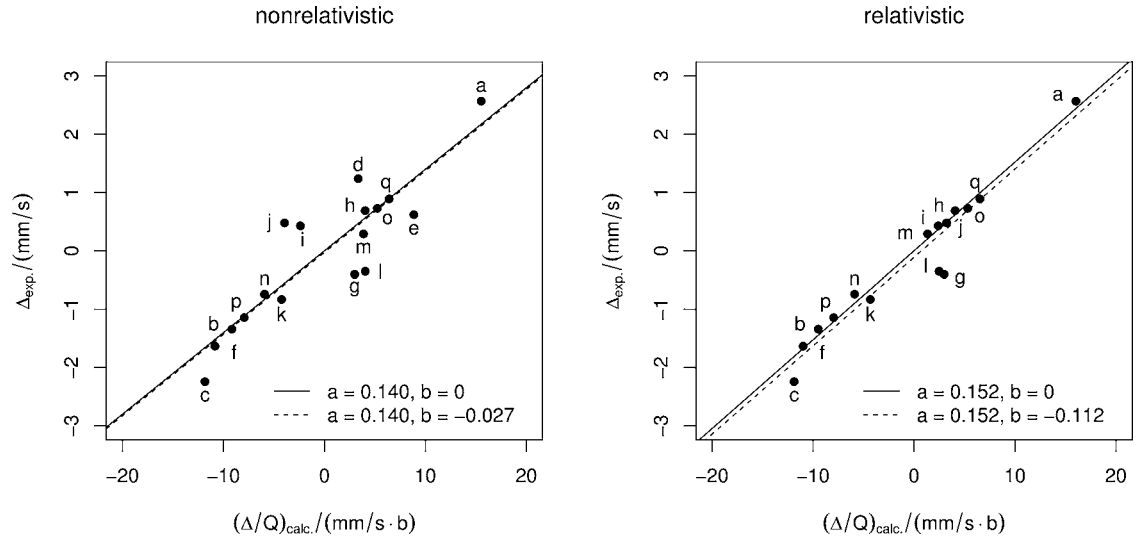

Figure 4. Linear regressions for the nonrelativistic (left panel) and relativistic (right panel) quadrupole splittings. The continuous line corresponds to the parametrization according to eq 6 with b = 0 mm/s; the dashed line displays the one according to eq 6 with variable b.

dx.doi.org/10.1021/ic4021349 | Inorg. Chem. 2013, 52, 14205−14215

Table 3. Calculated Isomer Shifts and Quadrupole Splittings for Possible Active-Site Models for Inhibited and Active [Fe] Hydrogenase[a]

OS	charge	L	X	Y	δ_{NR} (mm/s)	Δ_{NR} (mm/s)	δ_R (mm/s)	Δ_R (mm/s)
Fe(0)	−2	empty	S^-	OH	**0.05(1)**	1.18(16)	**0.04(1)**	1.39(11)
Experiment		CO			$\delta_{exp} = -0.03(1)$		$\Delta_{exp} = -1.38(2)$	
Fe(II)	−1	CO	S^-	O^-	**−0.03(2)**	**−1.21(16)**	**−0.04(2)**	**−1.32(10)**
Fe(II)	0	CO	S^-	OH	*0.00(1)*	**−1.40(18)**	**−0.01(1)**	**−1.52(12)**
Fe(II)	0	CO	SH	O^-	**−0.02(2)**	*−1.89(25)*	**−0.03(2)**	−2.08(16)
Fe(II)	+1	CO	SH	OH	0.04(1)	**−1.51(20)**	0.03(1)	*−1.64(13)*
Experiment		CN^-			$\delta_{exp} = 0.00(1)$		$\Delta_{exp} = -1.75(2)$	
Fe(II)	−2	CN^-	S^-	O^-	**−0.02(2)**	−1.32(17)	*−0.04(2)*	−1.47(12)
Fe(II)	−1	CN^-	S^-	OH	**0.02(1)**	−1.36(18)	**0.01(1)**	*−1.50(12)*
Fe(II)	−1	CN^-	SH	O^-	**0.01(1)**	**−1.91(25)**	**0.00(1)**	*−2.11(17)*
Fe(II)	0	CN^-	SH	OH	0.05(1)	**−1.77(23)**	0.04(1)	*−1.95(15)*
Experiment (95% N_2, 5% H_2)		?			$\delta_{exp} = 0.06(1)$		$\Delta_{exp} = 0.65(2)$	
Fe(II)	−1	H_2O	S^-	O^-	*0.03(1)*	**0.57(8)**	0.02(1)	**0.63(5)**
Fe(II)	0	H_2O	S^-	OH	**0.05(1)**	*0.55(7)*	*0.03(1)*	**0.62(5)**
Fe(II)	0	H_2O	SH	O^-	**0.07(1)**	0.97(13)	**0.06(1)**	1.07(8)
Fe(II)	+1	H_2O	SH	OH	0.11(1)	*0.49(7)*	0.10(1)	0.54(4)
Fe(II)	−1	H_2	S^-	O^-	0.01(1)	−0.93(12)	−0.01(1)	−1.03(8)
Fe(II)	0	H_2	S^-	OH	*0.03(1)*	−1.54(20)	0.02(1)	−1.68(13)
Fe(II)	0	H_2	SH	O^-	H_2 split and H^+ transferred to O^-			
Fe(II)	+1	H_2	SH	OH	**0.07(1)**	−1.65(22)	**0.06(1)**	−1.81(14)
Fe(II)	−2	H^-	S^-	O^-	−0.07(2)	−2.23(29)	−0.09(2)	−2.46(19)
Fe(II)	−1	H^-	S^-	OH	−0.03(2)	−2.16(28)	−0.05(2)	−2.38(19)
Fe(II)	−1	H^-	SH	O^-	−0.05(2)	−2.65(35)	−0.06(2)	−2.92(23)
Fe(II)	0	H^-	SH	OH	−0.01(1)	−2.59(34)	−0.02(2)	−2.85(22)
Fe(II)	−2	OH^-	S^-	O^-	0.00(1)	−1.10(15)	−0.01(2)	−1.19(9)
Fe(II)	−1	OH^-	SH	O^-	0.02(1)	−1.55(20)	0.01(1)	−1.70(13)
Fe(II)	−1	OH^-	S^-	OH	H^+ transferred from pyridol to hydroxo ligand			
Fe(II)	0	OH^-	SH	OH	H^+ transferred from pyridol to hydroxo ligand			
Fe(II)	0	empty	S^-	OH	−0.05(2)	*−0.71(9)*	−0.07(2)	−0.83(7)

[a] L, X, and Y refer to the positions depicted in Figure 2. The calculated values that match the experimental range (e.g., $\delta_{exp} = -0.03(1)$ means -0.03 ± 0.01 mm/s) within their standard deviation σ (given in parentheses) are given in bold face; those which match within 2σ are given in italics. The uncertainty in the calculated values is determined from the standard deviation of the adjustable parameters. Consequently, the deviations for the quadrupole splitting and isomer shift scale with the absolute value.

coordinated species features a dihydrogen arrangement which is a structural characteristic that might cause the significant deviation. Despite this discrepancy, the relative stability of the isomers is overall consistent, and our conclusions are not affected. For the sake of completeness, the B3LYP electronic energies are provided in the Supporting Information.

4. RESULTS AND DISCUSSION

4.1. Calibration. The linear regressions of the isomer shift as a function of the contact density, according to eq 3, are shown in Figure 3. Note that we were not able to converge the relativistic orbital optimization in the self-consistent field iterations for complexes d and e given our tight convergence thresholds. Therefore, the nonrelativistic reference set contains 17 molecules, and the relativistic reference set contains 15 molecules. The calculated contact densities correlate well with the experimental isomer shifts. The adjustable parameters, root-mean-square deviations (RMSD), and R^2 values are given in Table 2 (all structures as well as the contact density and EFG raw data have been collected in the Supporting Information). As expected, the contact density in the relativistic calculations is approximately 28% larger than that in the nonrelativistic case. However, the quality of the parametrization in terms of RMSD and R^2 values is about the same with slightly lower RMSD for the relativistic calculations. Based on the RMSD, the isomer shift can be predicted with an accuracy of about 0.04 mm/s.

The linear regressions for the quadrupole splitting are depicted in Figure 4. The parametrization to eq 6 with $b = 0$ mm/s yields essentially the same results as the parametrization with b as an adjustable parameter. Since b is an artificial parameter and does not improve the results, the approach with $b = 0$ mm/s is chosen for the reference calibration. The quality of the linear regression for the quadrupole splitting is worse compared with that for the isomer shift.[32] The RMSDs for the quadrupole splitting are larger than those for the isomer shift (see Table 2). Hence, based on the RMSD, the quadrupole splitting can be predicted to an accuracy of about 0.5 mm/s in nonrelativistic calculations and of about 0.3 mm/s in relativistic calculations. While R^2 for the nonrelativistic quadrupole splitting parametrization is 0.79, it is significantly better (R^2 = 0.93) for the relativistic results.

Note that for the nonrelativistic calibration of the quadrupole splitting, the constrained fit with $b = 0$ mm/s yields seemingly slightly more accurate results than the unconstrained fit, in which b is an adjustable parameter. This is because we have chosen $N_{free} = N_{sample} - N_{parameters}$ in the RMSD calculation and the number of parameters, $N_{parameters}$, will be just one if $b = 0$ mm/s (strictly speaking, the RMSD is defined through a division by the number of sample points, N_{sample}, (rather than by N_{free}), and thus our RMSD is more properly termed a standard deviation of the residuals).

dx.doi.org/10.1021/ic4021349 | Inorg. Chem. 2013, 52, 14205−14215

The value for the quadrupole moment Q (identical to slope a) obtained from the nonrelativistic fit (0.140 b) is at the lower bound compared with the value reported in the literature (0.150(20) b)[33] (note that this reference result is still subject of research and quadrupole moments have been reported ranging from 0.140(20)[90] to 0.160[91] and 0.170(10) b[92] for different methodologies; Pyykkö[93] gives a value of 0.160 b for a solid-state approach). The relativistic calculations yield a value of 0.152 b which is in good agreement with the literature values.

To compare the relativistic and nonrelativistic methodologies, the nonrelativistic parametrization was repeated with the same 15 molecules as are employed in the relativistic calibration (compare Table 2). The conclusions are essentially the same. The parametrizations for the isomer shift have about the same quality with the relativistic calculations being slightly better (now also in terms of R^2). The nonrelativistic quadrupole splitting parametrization becomes slightly better in terms of R^2 and RMSD with the reduced reference set, but it is still inferior to the relativistic results.

In general, we have observed small differences between nonrelativistic and relativistic results. This is surprising at first sight because by construction the relativistic model is better than the nonrelativistic one. And in fact, the significantly larger contact densities in the relativistic calculations are a clear sign for this. The fact that the nonrelativistic parametrization works so well is due to the molecule-specific differences in contact density and EFG brought about by the valence shell. Deficiencies in core-dominated contributions, which are well described in the relativistic but not in the nonrelativistic approach are absorbed in the regression parameters because these contributions are basically conserved atomic ones. As a consequence, the nonrelativistic calculations can be sensible because they are used to probe the valence shell rather then to provide correct raw data on the contact density.

4.2. Calculated Mössbauer Parameters for [Fe] Hydrogenase Active-Site Models. With the nonrelativistic and relativistic calibration parameters established, Mössbauer parameters for the [Fe] hydrogenase active-site models can be calculated. The resulting isomer shifts and quadrupole splittings for all active-site models considered and the experimental data available are collected in Table 3. The measured isomer shifts and quadrupole splittings of the enzyme incubated under 95% N_2/5% H_2 (δ_{exp} = 0.06 mm/s, Δ_{exp} = 0.65 mm/s), 100% H_2 (δ_{exp} = 0.06 mm/s, Δ_{exp} = 0.65 mm/s), and 100% H_2 + methenyl-H_4MPT$^+$ (0.7 mM) (δ_{exp} = 0.07 mm/s, Δ_{exp} = 0.67 mm/s) are similar and most probably stem from the same active-site species.[13] The species incubated under 100% N_2 atmosphere has only a slightly lower isomer shift (δ_{exp} = 0.04 mm/s, Δ_{exp} = 0.66 mm/s) and might be the same species as well.[13] In contrast to the CO and CN^- inhibited states, the identity of the ligand in position six of this resting state could not be determined in previous studies.

For the sake of brevity, the protonation states of the thiolate ligand and hydroxyl group are abbreviated as "(SA OB)", with A and B being either "H" for the protonated state or "−" for the deprotonated state. The term "species" refers to the ligand in position six, and the term "variant" denotes a distinct protonation state for a given species. The nonrelativistic and relativistic calculations yield similar results. Our discussion of the calculated Mössbauer parameters focuses on the results of the relativistic calculations. The Mössbauer parameters obtained with the nonrelativistic methodology are given for comparison because it can be considered as today's standard approach.

Which structural model fits best to the experimental data can be decided on the basis of the isomer shift and quadrupole splitting. For isomers (e.g., proton at S^- or O^-) also the relative electronic energy is considered. The accuracy of the assignment depends on the accuracy of the adjustable parameters discussed in section 4.1. The calculated uncertainty given in this section corresponds to the standard deviation σ obtained from error propagation of the uncertainties of the fitting parameters. For calculated Mössbauer parameters within the range of 2σ matching the range given by the experimental uncertainty, the corresponding calculated structures are considered to be a possible assignment to the experimentally measured Mössbauer parameters. The reliability of this assignment is further discussed in the next section.

The assignment of the oxidation state was another major difficulty in the experimental study because the measured isomer shift is atypically low for Fe(II) complexes (for instance, Fe(II) porphyrins have a much larger isomer shift).[13,94] In oxidation state Fe(0), we investigate active-site models in the protonation state (S^- OH). For all species with six ligands (L = H_2O, CO, CN^-, H_2, H^-), structure optimizations result in the dissociation of a ligand (in the case of L = H_2O and H_2, this is L; in all other cases, it is the thiolate ligand). Only the complex with an open coordination site in position six is stable, but it adopts a trigonal bipyramidal structure with a CO ligand in the apical position. Its isomer shift of 0.04(1) mm/s is in the range of the isomer shift of the unidentified species in the measurements (0.06(1) mm/s; see Table 3), but its quadrupole splitting is significantly too large (1.39(11) vs 0.65(2) mm/s in experiment). Hence, the Fe(0) species are either unstable or do not match the measured Mössbauer parameters. This is consistent with the accepted assignment of the oxidation state of +2 instead of 0.[5,13−15] Thus, the calculations clearly show that the isomer shifts measured in experiment[13] can be explained with model complexes in oxidation state +2.

We first discuss the CO and CN^- inhibited intermediates in oxidation state Fe(II). Here, the experimentally measured species are well-defined with either CO or CN^- being the ligand L at the sixth coordination site[7,13] (compare Table 3). The calculated isomer shifts and quadrupole splittings of the (S^- O^-) variant (δ_R = −0.04(2) mm/s, Δ_R = −1.32(10) mm/s) and the (S^- OH) variant of the CO inhibited complex (δ_R = −0.01(1) mm/s, Δ_R = −1.52(12) mm/s) are in the range of the experimental values (δ_{exp} = −0.03(1) mm/s, Δ_{exp} = −1.38(2) mm/s). The isomer shift of the (SH O^-) variant of −0.03(2) mm/s is in good agreement with experiment. However, its quadrupole splitting (−2.08(16) mm/s) is too large in absolute value. Furthermore, the (SH O^-) variant is 9.2 kJ/mol less stable than the (S^- OH) isomer. The variant with both groups protonated (SH OH) features a too large isomer shift but a quadrupole splitting that is still in the range of the experimental values. Hence, the protonation states (S^- O^-) and (S^- OH) could have been observed in experiment (given the experimental conditions of pH = 8,[13] the doubly deprotonated state (S^- O^-) might be formed).

For the CN^--coordinated complex, a similar pattern is observed. The isomer shift is sensitive to the protonation states of the two protic groups. With more negatively charged ligands (i.e., deprotonated ones), the isomer shift becomes more negative. The variants (S^- OH) (δ_R = 0.01(1) mm/s, Δ_R = −1.50(12) mm/s) and (SH O^-) (δ_R = 0.00(1) mm/s, Δ_R =

dx.doi.org/10.1021/ic4021349 | Inorg. Chem. 2013, 52, 14205−14215

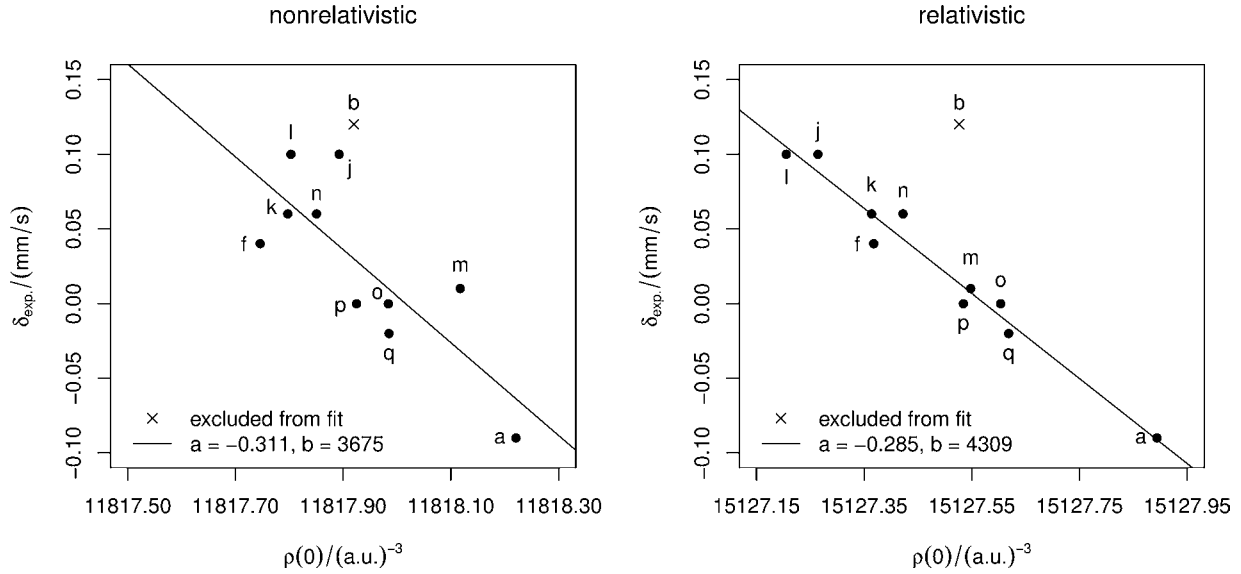

Figure 5. Linear regressions for the nonrelativistic (left panel) and relativistic (right panel) isomer shifts according to eq 3 with the training set reduced to the −0.1 to +0.1 mm/s range and with complex b excluded.

−2.11(17) mm/s) both have an isomer shift in good agreement with the experimental isomer shift (δ_{exp} = 0.00(1) mm/s) and their calculated quadrupole splittings are in the range of the experimental quadrupole splitting (Δ_{exp} = −1.75(2) mm/s). The (S^- OH) isomer is 54.2 kJ/mol more stable than the (SH O^-) isomer. The other two variants do not agree either in the quadrupole splitting ((S^- O^-), Δ_R = −1.47(12) mm/s) or in the isomer shift ((SH OH), δ_R = 0.04(1) mm/s). Hence, (S^- OH) and (SH O^-) are the most likely variants of the CN^- inhibited species in terms of Mössbauer parameters, but the former is energetically favored.

In order to assign the resting state structure measured in the presence of substrates and to identify the ligand L in position six by comparison to calculated Mössbauer parameters, several possible resting state structures were analyzed. They are collected in Table 3. We begin our discussion with the water-coordinated complex. The measured isomer shift of the enzyme incubated under 95% N_2/5% H_2 is δ_{exp} = 0.06(1) mm/s, and the quadrupole splitting is Δ_{exp} = 0.65(2) mm/s. The isomer shift of the (S^- OH) variant (δ_R = 0.03(1) mm/s) is in the range of the experimental value, and the quadrupole splitting (Δ_R = 0.62(5) mm/s) is in good agreement with experiment. The 15.7 kJ/mol less stable (SH O^-) variant has an isomer shift fitting to the measurement (δ_R = 0.06(1) mm/s), but the quadrupole splitting is too large (Δ_R = 1.07(8) mm/s). For the fully deprotonated variant (S^- O^-), the isomer shift is smaller than the measured value (δ_R = 0.02(1) mm/s) but the quadrupole splitting is in good agreement (Δ_R = 0.63(5) mm/s). The isomer shift of the (SH OH) variant (0.10(1) mm/s) does not match the experimental value, and the quadrupole splitting (0.54(4) mm/s) is smaller than the experimental range. Thus, the water complex, especially its (S^- OH) variant, is a likely candidate for the resting state. Its Mössbauer parameters also match the measurement for the species incubated under pure nitrogen atmosphere (δ_{exp} = 0.04(1) mm/s, Δ_{exp} = 0.66(2) mm/s).

In the H_2-coordinated species, optimization of the structure in protonation state (SH O^-) leads to spontaneous cleavage of H_2 with a proton transferred to O^-, in accord with a very low barrier for this process observed in previous work.[23] Hence, no Mössbauer parameters could be calculated for this variant. The (S^- O^-) and (S^- OH) variants feature calculated isomer shifts that are too small (−0.01(1) and 0.02(1) mm/s, respectively) compared with the measured isomer shift of 0.06(1) mm/s. The quadrupole splittings of (S^- O^-) and (S^- OH) are −1.03(8) and −1.68(13) mm/s, respectively, and thus too large in absolute value (Δ_{exp} = 0.65(2) mm/s). The isomer shift of the (SH OH) variant of 0.06(1) mm/s is in the range of the measured isomer shift, but its quadrupole splitting is significantly different (−1.81(14) mm/s). It is therefore unlikely that the measured species is a dihydrogen complex.

The hydride species can be excluded. The isomer shift is too small for all variants (from (S^- O^-) with −0.09(2) mm/s to (SH OH) with −0.02(2) mm/s). The negatively charged hydride is a strong donor and increases the electron density at the iron nucleus. The isomer shift becomes too negative, independent of the protonation state of the two protic groups. Also the calculated quadrupole splittings significantly differ from the measured quadrupole splitting (see Table 3). Remarkably, the (S^- OH) isomer is 59.2 kJ/mol more stable than the (SH O^-) isomer, possibly due to the Fe−$H^{\delta-}$···$H^{\delta+}$−O dihydrogen interaction.

With L being OH^-, the calculated isomer shifts are too small to correspond to the measured species ((S^- O^-) −0.01(2) mm/s and (SH O^-) 0.01(1) mm/s). The calculated quadrupole splittings are too large in absolute value ((S^- O^-) −1.19(9) mm/s and (SH O^-) −1.70(13) mm/s). For the (S^- OH) and (SH OH) variants, no Mössbauer parameters can be given because the proton of the pyridone's hydroxyl group is transferred to the OH^- ligand during structure optimization. For these reasons, OH^- can be excluded as a possible ligand to explain the experimental observations.

The uncoordinated species with an open coordination site in position six was only calculated in the (S^- OH) protonation state. Neither calculated isomer shift nor calculated quadrupole splitting do agree with experiment. The isomer shift of −0.07(2) mm/s strongly differs from the measured isomer shift of 0.06(1) mm/s, and the quadrupole splitting of −0.83(7) mm/s is too small (cf. Table 3). By comparison to the other results, it can be expected that the isomer shifts of the

dx.doi.org/10.1021/ic4021349 | Inorg. Chem. 2013, 52, 14205−14215

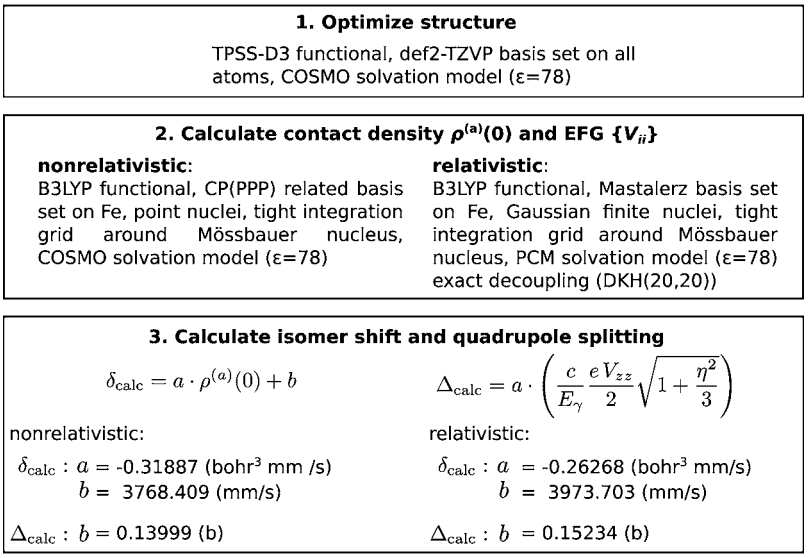

Figure 6. Flowchart of our computational scheme to calculate Mössbauer parameters.

other variants are significantly smaller than the measured value, too. Hence, this species can also be excluded.

To conclude, it is most likely that the water-coordinated species was measured in the (S^- OH) protonation state. The presence of the substrates (H_2 atmosphere and methenyl-H_4MPT^+ present in solution) or pure H_2 atmosphere do not lead to a change of the primary structure of the FeGP cofactor, which was already mentioned by Shima et al.[13] and is supported by the calculated Mössbauer parameters. This has implications for the mechanism proposed by Yang and Hall.[22] A significant amount of the product of H_2 cleavage (i.e., the H^- complex) is not measured in the presence of the substrates. We may speculate about the reasons. A possible rationale might be that the reaction proceeds via a different pathway not involving changes in the primary ligand sphere of Fe (outer-sphere mechanism). Another possible explanation is that the product of H_2 cleavage is only short-lived. The hydride transfer might be fast,[23] provided the hydride acceptor methenyl-H_4MPT^+ is present. Hence, it is possible that hydride cleavage only occurs in an arrangement where methenyl-H_4MPT^+ is already close to the iron atom and the hydride transfer can proceed directly after H_2 is cleaved, which would be in line with previous suggestions.[21]

4.3. Reliability of the Assignments. The training set for the isomer-shift calibration contains complexes with an isomer shift as large as 0.44 mm/s. The calculated isomer shifts of the [Fe] hydrogenase active-site model complexes are, however, in the range of −0.1 to +0.1 mm/s. To further elaborate on the reliability of our assignments in the previous section, the isomer-shift fitting procedure was repeated with complexes that have an isomer shift in the −0.1 to +0.1 mm/s range only. The resulting linear regression is presented in Figure 5. Complex b is excluded because it appears to be an outlier that points to a reinvestigation (Figure 5, right panel). With the relativistic methodology, the calibration in this region yields even more accurate parameters compared with the fit with the whole training set. The R^2 value of 0.97 and the RMSD of 0.011 mm/s indicate a higher accuracy (see Supporting Information for details). The assignments of variants based on this fit are as discussed before. Differences are found for the (S^- O^-) variant of the CO inhibited species, which has a too small isomer shift (−0.057(7) vs −0.03(1) mm/s experimentally), and the (S^- OH) variant of the water-coordinated species, whose isomer shift is too small as well (0.024(4) vs 0.06(1) mm/s experimentally). The isomer shift of the (S^- OH) variant of the water-coordinated species is, however, still in the range of the isomer shift of the species incubated under 100% N_2 (0.04(1) mm/s). Taking the RMSD as a criterion for the assignments leads to the same results. A detailed table of the calibration parameters and of the calculated Mössbauer parameters can be found in the Supporting Information. Importantly, the data scattering of the nonrelativistic calculations in the −0.1 to +0.1 mm/s range is much larger than for the data obtained with our relativistic methodology (compare the RMSDs). Fitting the nonrelativistic results in the −0.1 to +0.1 mm/s range leads to large errors in the fit parameters. Clearly, the relativistic methodology is more reliable.

In this work, the protein matrix surrounding the active site has been modeled by a continuum electrostatics approach. Modeling the effect of surrounding amino acid residues and solvent molecules by point charges derived from a force field, as it is done in mixed quantum-mechanical/molecular-mechanical (QM/MM) calculations (see for iron-porphyrins refs 95−99 or for Δ^9 desaturase ref 69), would clearly improve on the continuum description and can affect calculated Mössbauer parameters, especially the quadrupole splitting. Schöneboom et al.,[98] for example, reported differences of 0.04 mm/s in the isomer shift and of 0.7 mm/s in the quadrupole splitting for isolated-molecule versus QM/MM results for a highly polarized iron-oxo species. The size of the QM region can also affect the quadrupole splitting whereas the isomer shift appears to be more stable, as reported in a study on ribonucleotide reductase.[64] A QM/MM model for [Fe] hydrogenase to calculate Mössbauer parameters based on our calibration would be the next step, but clearly is beyond the scope of the present study and will be considered in future work.

5. CONCLUSION

Mössbauer parameters have been calculated for various model complexes of the active site of [Fe] hydrogenase in order to extract structural information about the CO and CN^- inhibited

states and about the resting state. In particular, the identity of the ligand in position six of the resting state and the protonation states of the thiolate ligand and of the pyridone's hydroxyl group have been investigated.

To achieve this goal, a new reference set of molecules has been compiled. Because calculated Mössbauer parameters are very sensitive to the computational methodology, state-of-the-art nonrelativistic and relativistic density functional theory methods have been calibrated against the reference set of experimentally known Mössbauer parameters. The local DLU approximation was invoked to make the decoupling of the Dirac Hamiltonian feasible. The latter was achieved by the Douglas–Kroll–Hess method up to 20th order in the orbitals and in the property operators. This novel approach allowed us to treat molecules of an unprecedented size with a large problem-adjusted basis set in a relativistic all-electron framework. While the nonrelativistic basis set has been chosen in accordance to Fe basis sets applied in such calculations in the literature, the relativistic basis set was chosen significantly larger. We found that the overall more consistent relativistic approach yields more accurate results for the quadrupole splitting. Moreover, in the relevant isomer-shift range from −0.1 to +0.1 mm/s significantly reduced data scattering is obtained. Our computational approach is schematically presented in Figure 6.

With this methodology, the measured Mössbauer parameters of the CO and CN^- inhibited states are reproduced by the calculations with an iron atom in the oxidation state +2. For the CO inhibited species, a protonated or deprotonated hydroxyl group and a thiolate ligand are most likely. Interestingly, for the CN^- inhibited species, the calculated parameters for a model with deprotonated hydroxyl group and a thiol ligand and of the isomer with protonated hydroxyl group and thiolate ligand are in the range of the measured values. The latter isomer is, however, energetically strongly favored. The structure of the resting state measured in the presence of the substrates and under pure H_2 atmosphere could not be unequivocally assigned in the experimental Mössbauer study.[13] Our results clearly favor H_2O as the ligand in position six with the hydroxyl group being protonated and a thiolate ligand as the most likely protonation state. All other possible ligands (H^-, H_2, OH^-) and an open coordination site can be excluded on the basis of the calculated Mössbauer parameters. The water-coordinated species appears to be the resting state also in the presence of the substrates. Hence, possible catalytic intermediates involving different coordination to iron must be short-lived.

To conclude, the quantum chemical method developed here has proven to be a valuable tool for the interpretation of Mössbauer measurements of [Fe] hydrogenase, and it will be as valuable for theoretical Mössbauer spectroscopy on Fe complexes in general.

■ ASSOCIATED CONTENT

Supporting Information

Additional material on the calculations and their validation, as well as the Cartesian coordinates of all complexes. This material is available free of charge via the Internet at http://pubs.acs.org.

■ AUTHOR INFORMATION

Corresponding Author

*E-mail: markus.reiher@phys.chem.ethz.ch.

Notes

The authors declare no competing financial interest.

■ ACKNOWLEDGMENTS

We gratefully acknowledge financial support by the Schweizerischer Nationalfonds (Project no. 200021L_138536).

■ REFERENCES

(1) Shima, S.; Thauer, R. K. *Chem. Rec.* **2007**, *7*, 37–46.
(2) Thauer, R. K.; Kaster, A.-K.; Goenrich, M.; Schick, M.; Hiromoto, T.; Shima, S. *Annu. Rev. Biochem.* **2010**, *79*, 507–536.
(3) Corr, M. J.; Murphy, J. A. *Chem. Soc. Rev.* **2011**, *40*, 2279–2292.
(4) Zirngibl, C.; Hedderich, R.; Thauer, R. K. *FEBS Lett.* **1990**, *261*, 112–116.
(5) Zirngibl, C.; van Dongen, W.; Schwörer, B.; von Bünau, R.; Richter, M.; Klein, A.; Thauer, R. K. *Eur. J. Biochem.* **1992**, *208*, 511–520.
(6) Schwörer, B.; Fernandez, V. M.; Zirngibl, C.; Thauer, R. K. *Eur. J. Biochem.* **1993**, *212*, 255–261.
(7) Lyon, E. J.; Shima, S.; Boecher, R.; Thauer, R. K.; Grevels, F.-W.; Bill, E.; Roseboom, W.; Albracht, S. P. *J. Am. Chem. Soc.* **2004**, *126*, 14239–14248.
(8) Shima, S.; Ataka, K. *FEBS Lett.* **2011**, *585*, 353–356.
(9) Tamura, H.; Salomone-Stagni, M.; Fujishiro, T.; Warkentin, E.; Meyer-Klaucke, W.; Ermler, U.; Shima, S. *Angew. Chem., Int. Ed.* **2013**, *52*, 9656–9659.
(10) Vignais, P. M.; Billoud, B. *Chem. Rev.* **2007**, *107*, 4206–4272.
(11) Fontecilla-Camps, J. C.; Volbeda, A.; Cavazza, C.; Nicolet, Y. *Chem. Rev.* **2007**, *107*, 4273–4303.
(12) Lyon, E. J.; Shima, S.; Buurman, G.; Chowdhuri, S.; Batschauer, A.; Steinbach, K.; Thauer, R. K. *Eur. J. Biochem.* **2004**, *271*, 195–204.
(13) Shima, S.; Lyon, E. J.; Thauer, R. K.; Mienert, B.; Bill, E. *J. Am. Chem. Soc.* **2005**, *127*, 10430–10435.
(14) Wang, X.; Li, Z.; Zeng, X.; Luo, Q.; Evans, D. J.; Pickett, C. J.; Liu, X. *Chem. Commun.* **2008**, *30*, 3555–3557.
(15) Salomone-Stagni, M.; Stellato, F.; Whaley, C. M.; Vogt, S.; Morante, S.; Shima, S.; Rauchfuss, T. B.; Meyer-Klaucke, W. *Dalton Trans.* **2010**, *39*, 3057–3064.
(16) Lubitz, W.; Reijerse, E.; van Gastel, M. *Chem. Rev.* **2007**, *107*, 4331–4365.
(17) Pilak, O.; Mamat, B.; Vogt, S.; Hagemeier, C. H.; Thauer, R. K.; Shima, S.; Vonrhein, C.; Warkentin, E.; Ermler, U. *J. Mol. Biol.* **2006**, *358*, 798–809.
(18) Shima, S.; Pilak, O.; Vogt, S.; Schick, M.; Stagni, M. S.; Meyer-Klaucke, W.; Warkentin, E.; Thauer, R. K.; Ermler, U. *Science* **2008**, *321*, 572–575.
(19) Hiromoto, T.; Ataka, K.; Pilak, O.; Vogt, S.; Stagni, M. S.; Meyer-Klaucke, W.; Warkentin, E.; Thauer, R. K.; Shima, S.; Ermler, U. *FEBS Lett.* **2009**, *583*, 585–590.
(20) Stiebritz, M. T.; Reiher, M. *Inorg. Chem.* **2010**, *49*, 5818–5823.
(21) Hiromoto, T.; Warkentin, E.; Moll, J.; Ermler, U.; Shima, S. *Angew. Chem., Int. Ed.* **2009**, *48*, 6457–6460.
(22) Yang, X.; Hall, M. B. *J. Am. Chem. Soc.* **2009**, *131*, 10901–10908.
(23) Finkelmann, A. R.; Stiebritz, M. T.; Reiher, M. *J. Phys. Chem. B* **2013**, *117*, 4806–4817.
(24) Gütlich, P.; Bill, E.; Trautwein, A. X. *Mössbauer Spectroscopy and Transition Metal Chemistry*; Springer: Heidelberg, 2011.
(25) Peng, D.; Reiher, M. *J. Chem. Phys.* **2012**, *136*, No. 244108.
(26) Filatov, M. *J. Chem. Phys.* **2007**, *127*, No. 084101.
(27) Mastalerz, R.; Lindh, R.; Reiher, M. *Chem. Phys. Lett.* **2008**, *465*, 157–164.
(28) Römelt, M.; Ye, S.; Neese, F. *Inorg. Chem.* **2009**, *48*, 784–785.
(29) Mastalerz, R.; Widmark, P.-O.; Roos, B. O.; Lindh, R.; Reiher, M. *J. Chem. Phys.* **2010**, *133*, No. 144111.
(30) Havlin, R. H.; Godbout, N.; Salzmann, R.; Wojdelski, M.; Arnold, W.; Schulz, C. E.; Oldfield, E. *J. Am. Chem. Soc.* **1998**, *120*, 3144–3151.

(31) Hopmann, K. H.; Ghosh, A.; Noodleman, L. *Inorg. Chem.* **2009**, *48*, 9155−9165.
(32) Bochevarov, A. D.; Friesner, R. A.; Lippard, S. J. *J. Chem. Theory Comput.* **2010**, *6*, 3735−3749.
(33) Martínez-Pinedo, G.; Schwerdtfeger, P.; Caurier, E.; Langanke, K.; Nazarewicz, W.; Söhnel, T. *Phys. Rev. Lett.* **2001**, *87*, No. 062701.
(34) Zhang, Y.; Mao, J.; Godbout, N.; Oldfield, E. *J. Am. Chem. Soc.* **2002**, *124*, 13921−13930.
(35) Zhang, Y.; Oldfield, E. *J. Phys. Chem. B* **2003**, *107*, 7180−7188.
(36) Han, W.-G.; Liu, T.; Lovell, T.; Noodleman, L. *J. Comput. Chem.* **2006**, *27*, 1292−1306.
(37) Sandala, G. M.; Hopmann, K. H.; Ghosh, A.; Noodleman, L. *J. Chem. Theory Comput.* **2011**, *7*, 3232−3247.
(38) Vrajmasu, V.; Münck, E.; Bominaar, E. L. *Inorg. Chem.* **2003**, *42*, 5974−5988.
(39) Sinnecker, S.; Slep, L. D.; Bill, E.; Neese, F. *Inorg. Chem.* **2005**, *44*, 2245−2254.
(40) Neese, F. *Inorg. Chim. Acta* **2002**, *337*, 181−192.
(41) Nemykin, V. N.; Hadt, R. G. *Inorg. Chem.* **2006**, *45*, 8297−8307.
(42) Shoji, M.; Saito, T.; Takeda, R.; Kitagawa, Y.; Kawakami, T.; Yamanaka, S.; Okumura, M.; Yamaguchi, K. *Chem. Phys. Lett.* **2007**, *446*, 228−232.
(43) Kurian, R.; Filatov, M. *J. Chem. Theory Comput.* **2008**, *4*, 278−285.
(44) Han, W.-G.; Noodleman, L. *Inorg. Chim. Acta* **2008**, *361*, 973−986.
(45) Edwards, P. R.; Johnson, C. E.; Williams, R. J. P. *J. Chem. Phys.* **1967**, *47*, 2074−2082.
(46) Fluck, E.; Kerler, W.; Neuwirth, W. *Angew. Chem., Int. Ed.* **1963**, *2*, 277−287.
(47) Herber, R. H.; Johnson, D. *Inorg. Chem.* **1979**, *18*, 2786−2790.
(48) Evans, D. J.; Hills, A.; Hughes, D. L.; Leigh, G. J. *Acta Crystallogr.* **1990**, *C46*, 1818−1821.
(49) Srivastava, K. K. P.; Sinha, T. P. *J. Phys. (Paris)* **1987**, *48*, 2119−2123.
(50) Obrist, B. V.; Chen, D.; Ahrens, A.; Schünemann, V.; Scopelliti, R.; Hu, X. *Inorg. Chem.* **2009**, *48*, 3514−3516.
(51) Chen, D.; Ahrens-Botzong, A.; Schünemann, V.; Scopelliti, R.; Hu, X. *Inorg. Chem.* **2011**, *50*, 5249−5257.
(52) Greatrex, R.; Greenwood, N. N. *Discuss. Faraday Soc.* **1969**, *47*, 126−135.
(53) Kukolich, S. G.; Roehrig, M. A.; Wallace, D. W.; Henderson, G. L. *J. Am. Chem. Soc.* **1993**, *115*, 2021−2027.
(54) Meyer, K.; Bill, E.; Mienert, B.; Weyhermüller, T.; Wieghardt, K. *J. Am. Chem. Soc.* **1999**, *121*, 4859−4876.
(55) Rohde, J.-U.; In, J.-H.; Lim, M. H.; Brennessel, W. W.; Bukowski, M. R.; Stubna, A.; Münck, E.; Nam, W.; Que, L. *Science* **2003**, *299*, 1037−1039.
(56) Burstyn, J. N.; Roe, J. A.; Miksztal, A. R.; Shaevitz, B. A.; Lang, G.; Valentine, J. S. *J. Am. Chem. Soc.* **1988**, *110*, 1382−1388.
(57) Li, M.; Bonnet, D.; Bill, E.; Neese, F.; Weyhermüller, T.; Blum, N.; Sellmann, D.; Wieghardt, K. *Inorg. Chem.* **2002**, *41*, 3444−3456.
(58) Chen, D.; Ahrens-Botzong, A.; Schünemann, V.; Scopelliti, R.; Hu, X. *Inorg. Chem.* **2011**, *50*, 5249−5257.
(59) Chen, D.; Scopelliti, R.; Hu, X. *J. Am. Chem. Soc.* **2010**, *132*, 928−929.
(60) Tao, J.; Perdew, J. P.; Staroverov, V. N.; Scuseria, G. E. *Phys. Rev. Lett.* **2003**, *91*, No. 146401.
(61) Weigend, F.; Ahlrichs, R. *Phys. Chem. Chem. Phys.* **2005**, *7*, 3297−3305.
(62) Grimme, S.; Antony, J.; Ehrlich, S.; Krieg, H. *J. Chem. Phys.* **2010**, *132*, No. 154104.
(63) Klamt, A.; Schüürmann, G. *J. Chem. Soc., Perkin Trans. 2* **1993**, 799−805.
(64) Han, W.-G.; Noodleman, L. *Theor. Chem. Acc.* **2010**, *125*, 305−317.
(65) Peterson, K. A.; Figgen, D.; Goll, E.; Stoll, H.; Dolg, M. *J. Chem. Phys.* **2003**, *119*, 11113−11123.
(66) TURBOMOLE V6.3 2011, a development of University of Karlsruhe and Forschungszentrum Karlsruhe GmbH, 1989−2007, TURBOMOLE GmbH, since 2007; available from http://www.turbomole.com.
(67) Ahlrichs, R.; Bär, M.; Häser, M.; Horn, H.; Kölmel, C. *Chem. Phys. Lett.* **1989**, *162*, 165−169.
(68) Weigend, F. *Phys. Chem. Chem. Phys.* **2006**, *8*, 1057−1065.
(69) Srnec, M.; Rokob, T. A.; Schwartz, J. K.; Kwak, Y.; Rulíšek, L.; Solomon, E. I. *Inorg. Chem.* **2012**, *51*, 2806−2820.
(70) Knecht, S.; Fux, S.; van Meer, R.; Visscher, L.; Reiher, M.; Saue, T. *Theor. Chem. Acc.* **2011**, *129*, 631−650.
(71) Aquilante, F.; De Vico, L.; Ferré, N.; Ghigo, G.; Malmqvist, P.-Å.; Neogrády, P.; Pedersen, T. B.; Pitoňák, M.; Reiher, M.; Roos, B. O.; Serrano-Andrés, L.; Urban, M.; Veryazov, V.; Lindh, R. *J. Comput. Chem.* **2010**, *31*, 224−247.
(72) Lee, C.; Yang, W.; Parr, R. G. *Phys. Rev. B* **1988**, *37*, 785−789.
(73) Becke, A. D. *J. Chem. Phys.* **1993**, *98*, 5648−5652.
(74) Stephens, P. J.; Devlin, F. J.; Chabalowski, C. F.; Frisch, M. J. *J. Phys. Chem.* **1994**, *98*, 11623−11627.
(75) Vosko, S. H.; Wilk, L.; Nusair, M. *Can. J. Phys.* **1980**, *58*, 1200−1211.
(76) Fux, S. Ph.D. thesis, ETH, Diss. No. 20112, 2011.
(77) Lindh, R.; Malmqvist, P.-Å.; Gagliardi, L. *Theor. Chem. Acc.* **2001**, *106*, 178−187.
(78) Barone, V.; Cossi, M. *J. Phys. Chem. A* **1998**, *102*, 1995−2001.
(79) Cossi, M.; Rega, N.; Scalmani, G.; Barone, V. *J. Chem. Phys.* **2001**, *114*, 5691−5701.
(80) Roos, B. O.; Lindh, R.; Malmqvist, P.-A.; Veryazov, V.; Widmark, P.-O. *J. Phys. Chem. A* **2004**, *108*, 2851−2858.
(81) Reiher, M.; Wolf, A. *J. Chem. Phys.* **2004**, *121*, 2037.
(82) Reiher, M.; Wolf, A. *J. Chem. Phys.* **2004**, *121*, 10945.
(83) Wolf, A.; Reiher, M. *J. Chem. Phys.* **2006**, *124*, No. 064102.
(84) Wolf, A.; Reiher, M. *J. Chem. Phys.* **2006**, *124*, No. 064103.
(85) Mastalerz, R.; Barone, G.; Lindh, R.; Reiher, M. *J. Chem. Phys.* **2007**, *127*, No. 074105.
(86) Peng, D.; Hirao, K. *J. Chem. Phys.* **2009**, *130*, No. 044102.
(87) Peng, D.; Reiher, M. *Theor. Chem. Acc.* **2012**, *131*, 1081.
(88) Autschbach, J.; Peng, D.; Reiher, M. *J. Chem. Theory Comput.* **2012**, *8*, 4239−4248.
(89) Reiher, M.; Wolf, A. *Relativistic Quantum Chemistry*; Wiley-VCH: Weinheim, Germany, 2009.
(90) Schwerdtfeger, P.; Söhnel, T.; Pernpointner, M.; Laerdahl, J. K.; Wagner, F. E. *J. Chem. Phys.* **2001**, *115*, 5913−5924.
(91) Dufek, P.; Blaha, P.; Schwarz, K. *Phys. Rev. Lett.* **1995**, *75*, 3545−3548.
(92) Wdowik, U. D.; Ruebenbauer, K. *Phys. Rev. B* **2007**, *76*, No. 155118.
(93) Pyykkö, P. *Mol. Phys.* **2008**, *106*, 1965−1974.
(94) Debrunner, P. *Iron Porphyrins*; Wiley-VCH: Weinheim, Germany, 1989; Part 3, pp 137−234.
(95) Cho, K.-B.; Hirao, H.; Chen, H.; Carvajal, M. A.; Cohen, S.; Derat, E.; Thiel, W.; Shaik, S. *J. Phys. Chem. A* **2008**, *112*, 13128−13138.
(96) Derat, E.; Cohen, S.; Shaik, S.; Altun, A.; Thiel, W. *J. Am. Chem. Soc.* **2005**, *127*, 13611−13621.
(97) Lai, W.; Chen, H.; Cho, K.-B.; Shaik, S. *J. Phys. Chem. A* **2009**, *113*, 11763−11771.
(98) Schöneboom, J. C.; Neese, F.; Thiel, W. *J. Am. Chem. Soc.* **2005**, *127*, 5840−5853.
(99) Altun, A.; Thiel, W. *J. Phys. Chem. B* **2005**, *109*, 1268−1280.